# Phase-matching analysis in high-order harmonic generation with nonzero orbital angular momentum Laguerre-Gaussian beams

Cheng Jin [1,2,*], Baochang Li,[1] Kan Wang,[1] Chenhui Xu,[1] Xiangyu Tang,[1] Chao Yu,[1] and C. D. Lin [2]

[1]*Department of Applied Physics, Nanjing University of Science and Technology, Nanjing, Jiangsu 210094, China*
[2]*J. R. Macdonald Laboratory, Department of Physics, Kansas State University, Manhattan, Kansas 66506, USA*

Through high-order harmonic generation driven by intense ultrashort vortex infrared or midinfrared lasers, a nonzero orbital angular momentum can be imprinted onto extreme ultraviolet (XUV) or soft-x-ray (SXR) light pulses. Here we simulate the generation of vortex XUV harmonics in the gas medium as well as their propagation in vacuum till reaching the far field. We find that the intensity and phase of generated high harmonics are very sensitive to the position of gas jet with respect to the laser focus. The topological charge of the $q$th harmonic is found to be $q$ times that of the driving Laguerre-Gaussian beam. Each harmonic in the far field appears as a single ring in the transverse plane with an invariant diameter which is scalable with the fundamental topological charge only when the gas jet is placed after the laser focus. The underlying phase-matching mechanism is analyzed by examining the spatial map of the coherence length and by calculating the evolution of harmonic emission in the medium. We anticipate this work to stimulate interest in generating intense vortex XUV or SXR attosecond pulses for probing dynamics of molecules where special molecular features are difficult to be detected with linear or circular XUV or SXR pulses.

## I. INTRODUCTION

An optical vortex is a light beam with helical phase that possesses a spiral wave front [1–3]. The azimuthal phase change of the wave front around the propagation axis is $2\pi l$, thus carrying an orbital angular momentum (OAM) of $l\hbar$ per photon, where $\hbar$ is the reduced Planck constant and the vortex light beam is said to have a topological charge $l$. In a light-matter interaction, the OAM can be transferred to matter, such as in atomic and molecular systems [4–7]. A prominent example of such a vortex field is a Laguerre-Gaussian (LG) beam with OAM, which is related to the annular spatial profile with a null central region, first demonstrated in a pioneering work by Allen *et al.* in 1992 [8]. Due to the unique features of the vortex beam, it has been applied to numerous different fields, including optical manipulation [9], quantum information processing [10], optical communications [11], phase-contrast interferometry [12], chiral recognition in molecules [13,14], and so on.

In the infrared (IR) and visible spectral range, light beams with OAM can be created with optical elements [2]; it is quite difficult to use the same technology to create vortex extreme ultraviolet (XUV) or soft-x-ray (SXR) beams though [15]. However, using the up-conversion process of high-order harmonic generation (HHG) by an intense ultrashort vortex IR pulse interacting with a gaseous [16,17] or solid medium [18], vortex XUV beams have been reported. The first experiment was performed by Zürch *et al.* [19] in 2012. It was found that low-charged XUV vortices are generated but the phase

of harmonic does not scale with harmonic order. Soon after, Gariepy *et al.* [20] measured the transverse phase of the generated vortex harmonics with interferometric technique. They found that the topological charge of each harmonic is $q$ times ($q$ is the harmonic order) the topological charge of the driving laser. Since then, other experimental studies have been carried out focusing on characterizing attosecond vortex pulses and generating helical electron bursts [21], controlling the HHG topological charge by mixing two-color driving beams in a noncollimated scheme [22,23], creating radially and azimuthally polarized beams [24], generating time-varying OAM in the HHG [16], and others [25,26].

To fully understand experimentally measured vortex harmonics generated in a gas using theoretical simulations, one needs to consider both the generation at the single-atom level and the propagation of the harmonic field in the macroscopic medium, including its propagation in free space. The former can be obtained by solving the time-dependent Schrödinger equation (TDSE), or by some simpler models. In the first theoretical study on the vortex HHG by Hernández-García *et al.* [27], the single-atom response was calculated with the improved strong-field approximation (SFA), called SFA+. By treating the gas target as discretized elementary radiators, the harmonic emissions were computed with an electromagnetic field propagator. This method was then applied to study quantum-path signatures in attosecond helical beams [28], harmonics generated by nonpure vortex modes [29], and generation of fractional OAM beams [30]. Later, Paufler *et al.* [31,32] used the Fraunhofer diffraction formula to calculate harmonic emissions with tailored OAM in the far field. With these approaches, the significance of various mechanisms and their interplays for the formation and evolution of

*Corresponding author: cjin@njust.edu.cn

harmonic field in the gas medium cannot be demonstrated. Interestingly, to treat phase matching, the standard method of solving the three-dimensional (3D) Maxwell's wave equations for non-OAM beams [33–38] has rarely been applied to high harmonics generated with intense vortex IR pulses [21,39,40].

In this work, our main goal is to present a complete theoretical analysis of the generation of high harmonics with OAM, thus identifying how the different factors affect the phase-matching conditions, which determine the amplitude and phase of the vortex harmonics in the XUV regime. The theory includes the solution of the 3D Maxwell's wave equations for the propagation of harmonic field in the medium, the quantitative rescattering (QRS) model for the single-atom response, and Huygens' integral under the paraxial approximation for the far-field harmonic emission. We will investigate the characteristics of intensity and phase of vortex harmonics in both the near and far fields driven by LG beams by varying the position of gas medium with respect to the laser focus, and will analyze the spatial coherence length and the accumulated field strength of high harmonics in the medium. The vortex harmonics generated with different fundamental topological charges will also be discussed.

## II. THEORETICAL METHODS

To calculate high harmonics generated inside a gas medium driven by an OAM laser beam, two parts have to be accounted for as follows. (i) Single-atom response in which each atom interacts with a local field at a given spatial position of the OAM beam. The laser-atom interaction can be treated under the dipole approximation [41]. (ii) Macroscopic response, in which responses from atoms within the interaction region are added up coherently. The near-field harmonics emitted at the exit of the gas medium continue to propagate in vacuum using Huygens' integral until they reach the detector where far-field harmonics are obtained.

### A. Propagation equations of high-harmonic field

We assume the fundamental beam with OAM is not modified within the ionized gas medium, i.e., it propagates as in free space. This is valid when laser intensity is low and gas pressure is low. The propagation of vortex harmonic field in the ionizing medium is governed by (in a Cartesian coordinate) [42]

$$\nabla^2 E_h(x, y, z, t) - \frac{1}{c^2} \frac{\partial^2 E_h(x, y, z, t)}{\partial t^2} = \mu_0 \frac{\partial^2 P_{nl}(x, y, z, t)}{\partial t^2},$$
(1)

where

$$P_{nl}(x, y, z, t) = [n_0 - n_e(x, y, z, t)]D(x, y, z, t) \quad (2)$$

and

$$n_e(t) = n_0 \left\{ 1 - \exp\left[ -\int_{-\infty}^{t} w(\tau) d\tau \right] \right\}. \quad (3)$$

Here, $P_{nl}(x, y, z, t)$ is the nonlinear polarization, $n_0$ is the neutral atom density, $n_e(x, y, z, t)$ is the free electron density, and $w(\tau)$ is the tunnel ionization rate. The induced dipole moment

$D(x, y, z, t)$ is calculated in the local laser field. Effects of absorption and free electron dispersion are neglected.

By employing a moving coordinate frame ($z' = z$ and $t' = t - z/c$) and applying paraxial approximation (i.e., neglecting the $\partial^2 E_h/\partial z'^2$ term), one obtains

$$\nabla_\perp^2 E_h(x, y, z', t') - \frac{2}{c} \frac{\partial^2 E_h(x, y, z', t')}{\partial z' \partial t'} = \mu_0 \frac{\partial^2 P_{nl}(x, y, z', t')}{\partial t'^2}.$$
(4)

In this equation, the transverse Laplace operator $\nabla_\perp^2 = \partial^2/\partial x^2 + \partial^2/\partial y^2$.

Using Fourier transform, the temporal derivative in Eq. (4) can be eliminated and

$$\nabla_\perp^2 \widetilde{E}_h(x, y, z', \omega) - \frac{2i\omega}{c} \frac{\partial \widetilde{E}_h(x, y, z', \omega)}{\partial z'}$$
$$= -\mu_0 \omega^2 \widetilde{P}_{nl}(x, y, z', \omega), \quad (5)$$

where

$$\widetilde{E}_h(x, y, z', \omega) = \widehat{F}[E_h(x, y, z', t')] \quad (6)$$

and

$$\widetilde{P}_{nl}(x, y, z', \omega) = \widehat{F}[P_{nl}(x, y, z', t')]. \quad (7)$$

Here $\widehat{F}$ is the Fourier transform operator acting on the temporal coordinate.

An operator-splitting method is used to solve Eq. (5). The advance of electric field from $z'$ to $z' + \triangle z'$ is separated in two steps:

$$\frac{\partial \widetilde{E}_h(x, y, z', \omega)}{\partial z'} = -\frac{ic}{2\omega} \nabla_\perp^2 \widetilde{E}_h(x, y, z', \omega) \quad (8)$$

and

$$\frac{\partial \widetilde{E}_h(x, y, z', \omega)}{\partial z'} = -\frac{ic\mu_0\omega}{2} \widetilde{P}_{nl}(x, y, z', \omega). \quad (9)$$

Once the harmonic field at the exit plane of gas medium ($z' = z_{\text{out}}$) is computed, the total HHG power spectrum is obtained by integrating over the transverse plane:

$$S_h(\omega) \propto \int_{-\infty}^{\infty} \int_{-\infty}^{\infty} |\widetilde{E}_h(x, y, z', \omega)|^2 dx \, dy. \quad (10)$$

### B. Fundamental Laguerre-Gaussian beams

For the fundamental driving laser, we employ a Laguerre-Gaussain (LG) beam. Under the paraxial and slowly varying transverse amplitude approximations, its electric field can be expressed in cylindrical coordinates as

$$LG_{l,p}(r, \phi, z')$$
$$= E_0 \frac{w_0}{w(z')} \left( \frac{r}{w(z')} \right)^{|l|} L_p^{|l|} \left( \frac{2r^2}{w^2(z')} \right) \exp\left( -\frac{r^2}{w^2(z')} \right)$$
$$\times \exp\left( -ik_0 \frac{r^2}{2R(z')} - i\zeta(z') - il\phi \right). \quad (11)$$

Note that the above expression is written in the moving frame; thus the factor of $\exp(-ik_0z)$ in the rest frame was omitted. The negative sign in the phase is consistent with the convention of Fourier transform in Eq. (5) [32]. In Eq. (11), $w_0$ is the beam waist at the focus, $w(z') = w_0\sqrt{1 + (z'/z_0)^2}$ is the
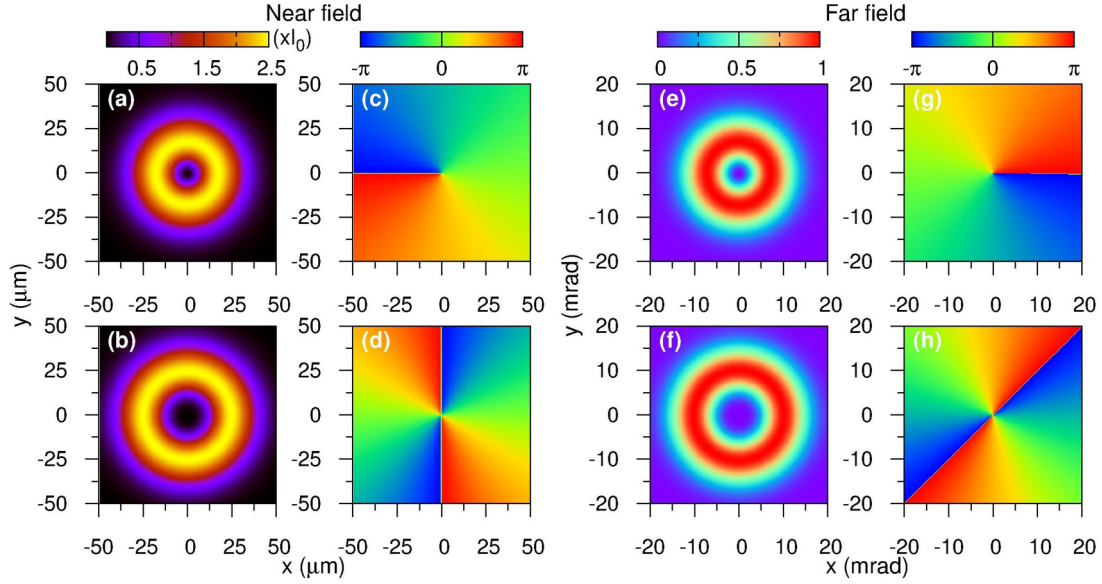
FIG. 1. Left: intensity [(a) and (b)] and phase [(c) and (d)] of the transverse profiles of the fundamental LG beams at the focus position ($z' = 0$) (the near field). Beam waist $w_0 = 25\ \mu$m; peak intensity is $2.5 \times 10^{14}$ W/cm$^2$. $I_0 = 10^{14}$ W/cm$^2$. Right: Intensity [(e) and (f)] and phase [(g) and (h)] distributions in the far field ($z' = +\infty$). Intensity has been normalized. Upper row: LG$_{1,0}$ mode; lower row: LG$_{2,0}$ mode. The phase is defined from $-\pi$ to $\pi$.

beam width, and $z_0 = \pi w_0^2 / \lambda_0$ is the Rayleigh length with the laser wavelength $\lambda_0$. $L_p^{|l|}(x)$ is the associated Laguerre polynomial. $R(z') = z'[1 + (z_0/z')^2]$ is the radius of curvature of the wave front and Gouy phase is given by $\zeta(z') = -(|l| + 2p + 1)\arctan(z'/z_0)$. The index $l = 0, \pm 1, \pm 2, \ldots$ gives the topological charge and $p = 0, 1, 2, \ldots$ is associated with the number of radial nodes.

We consider two LG beams with $l = 1$ and $l = 2$ while $p = 0$. Laser wavelength is 800 nm and the beam waist is $w_0 = 25\ \mu$m; thus the Rayleigh range $z_0 = 2.45$ mm. By properly adjusting the amplitude of the field $E_0$, the peak intensity at focus is set as $2.5 \times 10^{14}$ W/cm$^2$. The intensity and phase distributions are shown in Fig. 1. At the laser focus ($z' = 0$), because the radial node is set to zero, there is only one ring in Figs. 1(a) and 1(b), respectively. The term $\exp(-il\phi)$ in Eq. (11) imprints an azimuthal phase variation of $2\pi$ and $4\pi$ on the beams in Figs. 1(c) and 1(d), respectively. In these plots the range of phase is defined within $[-\pi : \pi]$. In the far field ($z' = +\infty$), the intensity profiles remain the same as those at focus. However, the phase distributions are varied; see Figs. 1(g) and 1(h). This is due to the shift of Gouy phase $\zeta(z')$. From $z' = 0$ to $+\infty$, the phase shift is $-\pi$ (or $-3\pi/2$) for LG$_{1,0}$ (or LG$_{2,0}$) mode. One can also see that the radius of the maximum intensity ring for LG$_{2,0}$ mode is $\sqrt{2}$ times larger than that for LG$_{1,0}$ mode, in both near and far fields. This can be derived from Eq. (11) that the radial coordinate of maximum intensity of a LG$_{l,0}$ beam is at $r_{l,\max}(z') = w(z')\sqrt{|l|/2}$.

### C. Separation of spatial and temporal dependence in the nonlinear polarization

The spatial electric field of the LG beam in Eq. (11) can be simply expressed as

$$LG_{l,p}(r, \phi, z') = \varepsilon(r, z')e^{i\varphi_l(r,\phi,z')}, \quad (12)$$

where $\varepsilon(r, z')$ is the amplitude of the field and $\varphi_l(r, \phi, z')$ is the phase. The spatiotemporal electric field of a linearly polarized ultrashort laser pulse is written as

$$E(r, \phi, z', t') = \mathrm{Re}[\varepsilon(r, z')e^{i\varphi_l(r,\phi,z')}A(t')e^{i(\omega_0 t' + \varphi_{\mathrm{cep}})}], \quad (13)$$

where $\omega_0$ is the central frequency, $A(t')$ is the temporal envelope, and the carrier envelope phase is represented by $\varphi_{\mathrm{cep}}$.

To separate the temporal and spatial dependence in Eq. (13), we define a new time frame as

$$t'' = t' + \varphi_l(r, \phi, z')/\omega_0. \quad (14)$$

Then the electric field becomes

$$E(r, z', t'') = \varepsilon(r, z')A(t'')\cos(\omega_0 t'' + \varphi_{\mathrm{cep}}). \quad (15)$$

Here we ignore any time shift in the temporal envelope $A(t')$, which is valid for a long-duration pulse. The spatial dependence can be reduced to the dependence of peak field only.

Using the time frame $t''$, the nonlinear polarization of Eq. (7) in the moving frame can be rewritten as

$$\widetilde{P}_{nl}(r, \phi, z', \omega) = \widehat{F}[P_{nl}(r, \phi, z', t')]$$
$$= \widehat{F}[P_{nl}(r, z', t'')]e^{i(\omega/\omega_0)\varphi_l(r,\phi,z')}. \quad (16)$$

In the calculation, we first compute $P_{nl}(r, z', t'')$ for a number of laser peak intensities. When we solve Eq. (5), the nonlinear polarization in the $t''$ frame can be obtained by interpolating the peak intensity $|\varepsilon(r, z')|^2$. As seen in Eq. (16), a harmonic-order dependent factor, which accounts for the effect of the laser geometric phase, is added to restore the moving frame. Note that the use of the interpolation method greatly improves the computation efficiency for the propagation of harmonic fields.

### D. Far-field harmonic emission

Once the high harmonics are emitted from the exit face of a gas medium at $z' = z_{out}$ (near field), they further propagate in vacuum. The far-field harmonic emissions can be obtained from near-field ones by using Huygens' integral under the paraxial and Fresnel approximations (in a Cartesian coordinate) as [43]

$$
\begin{aligned}
&E_h^f(x_f, y_f, z_f, \omega) \\
&= (ik/2\pi L) \iint \tilde{E}_h(x, y, z_{out}, \omega) \\
&\times \exp\left\{ -(ik/2L)[(x_f - x)^2 + (y_f - y)^2] \right\} dx\, dy, \quad (17)
\end{aligned}
$$

where $L = z_f - z_{out}$, $z_f$ is the far-field position from the laser focus, $x_f$ and $y_f$ are the transverse coordinates in the far field, and the wave vector $k$ is given by $k = \omega/c$. Note that Eq. (17) is used to calculate the harmonic field on a plane at $z_f$ perpendicular to the propagation axis, while far-field harmonics are computed in a spherical surface with a radius $L$. Note that Eq. (17) gives an equivalent solution of Eq. (5) in vacuum for each $\omega$.

### E. Quantitative rescattering model for single-atom response

Since polarization of the laser pulse is linear, single-atom induced dipole moment $D(t)$ in Eq. (2) can be accurately calculated by using the quantitative rescattering (QRS) model [44,45]. In this model, the $D(t)$ is given in the frequency domain $D(\omega)$, which can be written as [44,46]

$$
D(\omega) = \sqrt{N} W(\omega) d(\omega), \quad (18)
$$

where $N$ is the ionization probability taken at the end of the laser pulse, $d(\omega)$ is the complex photorecombination (PR) transition dipole matrix element, and $W(\omega)$ is the complex microscopic wave packet. The QRS improves the strong-field approximation (SFA) by replacing the plane wave used in the SFA with accurate scattering wave in the PR transition dipole matrix elements, while the returning wave packet is the same as that in the SFA. In practical applications, the QRS obtains the induced dipole moment by

$$
D^{qrs}(\omega) = D^{sfa}(\omega) \sqrt{\frac{N^{qrs}}{N^{sfa}}} \frac{d^{qrs}(\omega)}{d^{sfa}(\omega)}, \quad (19)
$$

where both $D^{sfa}(\omega)$ and $d^{qrs}(\omega)$ are complex numbers, while $d^{sfa}(\omega)$ is either a pure real or pure imaginary number. $N^{qrs}$ is calculated by using the ADK theory [47,48]. Within the single active electron (SAE) approximation, $d^{qrs}(\omega)$ can be calculated by using "exact" numerical wave functions for the bound and continuum states. For Ar, the atomic potential takes the following form [48]:

$$
V(r) = -\frac{Z_c + a_1 e^{-a_2 r} + a_3 r\, e^{-a_4 r} + a_5 e^{-a_6 r}}{r}, \quad (20)
$$

where $Z_c$ is the charge seen by the active electron asymptotically and $a_1, \ldots, a_6$ are parameters obtained by fitting $V(r)$ to the numerical potential from self-interaction free density functional theory. Using such a single electron model, the
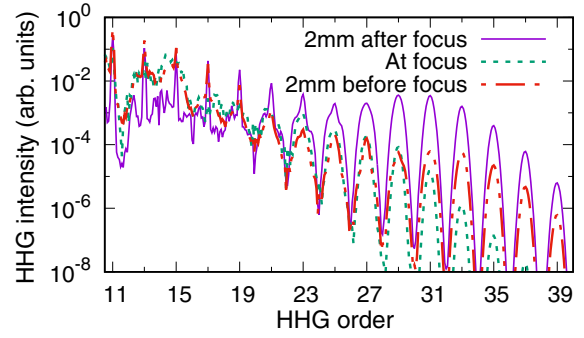


FIG. 2. Simulated macroscopic harmonic spectra integrated over the exit plane of the gas medium generated with a $LG_{1,0}$ beam. The gas jet is taken at three positions as indicated. The peak intensity at the center of the gas medium is fixed at $1.5 \times 10^{14}$ W/cm$^2$. See text for additional laser parameters.

minimum in the calculated PR transition dipole for Ar occurs at 40 eV [42].

## III. HIGH-HARMONIC GENERATION WITH LAGUERRE-GAUSSIAN BEAM ($l = 1$, $p = 0$)

### A. Dependence of total harmonic spectra on the position of gas jet

In our simulation, we first take the fundamental laser to be a $LG_{1,0}$ beam. The beam waist at the focus is fixed as $w_0 = 25$ $\mu$m, which is considered to be tightly focused. The pulse is linearly polarized, with wavelength at 800 nm, pulse duration at 10 optical cycles (26.7 fs), and $\varphi_{cep}$ at 0. The laser pulse interacts with a uniformly distributed Ar gas jet with length of 1 mm. Typically, in the calculation we discretize the space in the transverse direction using 500 grid points and the longitudinal direction 400 grid points.

We consider three cases where the center of the gas jet is placed at 2 mm after, at, or 2 mm before the laser focus, respectively. The peak intensity at the center is always fixed at $1.5 \times 10^{14}$ W/cm$^2$. The simulated total HHG spectra calculated by Eq. (10) are shown in Fig. 2. There are two most notable features when the gas jet is located 2 mm after the laser focus: (i) it has the best well-resolved odd harmonics and (ii) it has the most flat plateau and the most efficient generation of higher-order harmonics. These are similar to harmonic generation by using a Gaussian beam without OAM [42].

### B. Intensity and phase distributions of high harmonics in the near and far fields

For the three gas-jet positions above, in Figs. 3, 4, and 5, we show the intensity and phase distributions in space for two selected harmonics in the plateau region and one harmonic at the cutoff. Both near- and far-field harmonics are considered. We first take a close look of Fig. 3 where the gas jet is placed after laser focus. In the near field, the harmonic intensity is distributed over one single ring primarily, see Figs. 3(a)–3(c), and the phase distributions in Figs. 3(d)–3(f) do not show any nodes along the radial direction. Over one circle, we can identify that the phase change of $2\pi q$ and thus the topological charge is $q$ for the $q$th harmonic. In the far field, there is one
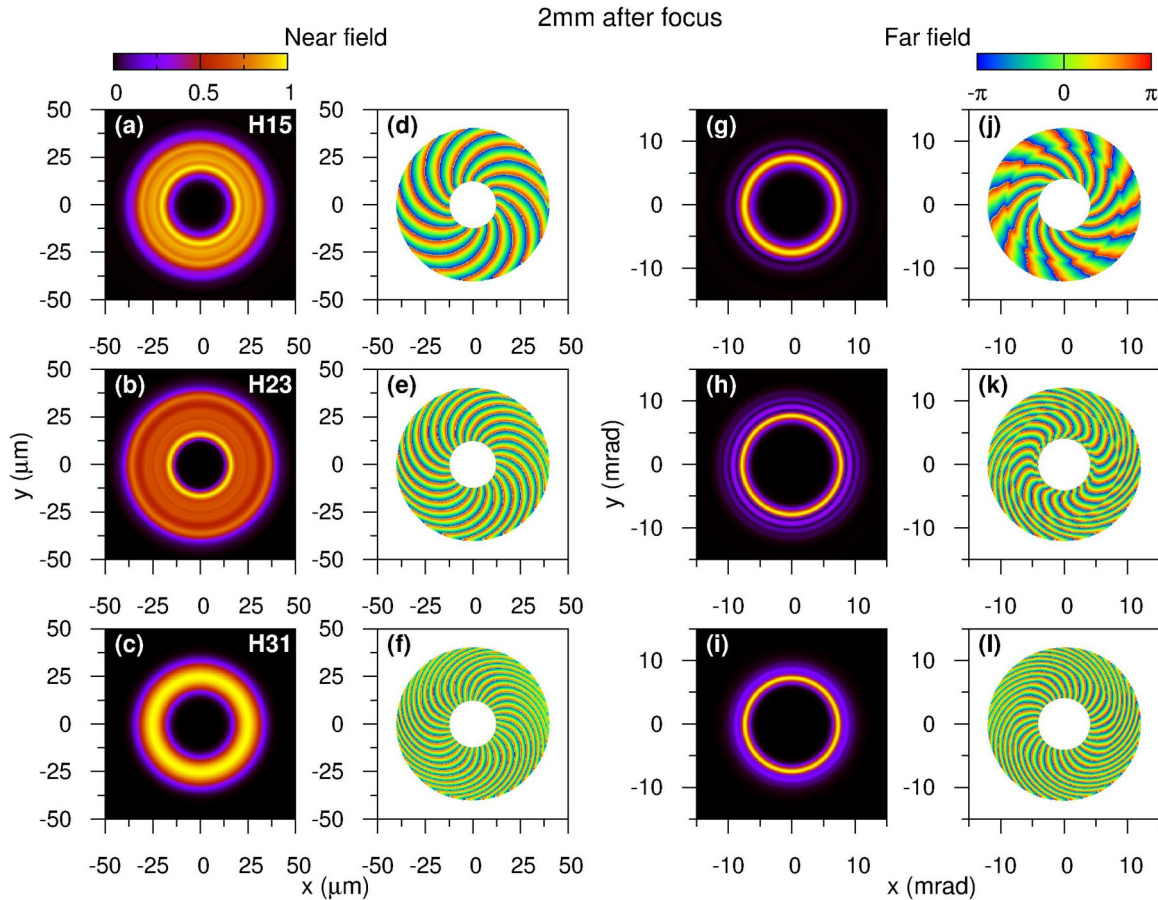
FIG. 3. Left: intensity [(a)–(c)] and phase [(d)–(f)] distributions of high harmonics generated with a $LG_{1,0}$ beam in the near field (at the exit plane of the gas medium). Right: angular profiles of the intensity [(g)–(i)] and phase [(j)–(l)] of high harmonics in the far field. First row: 15th-order harmonic (H15); second row: H23; third row: H31. The intensity in the near and far fields are normalized separately. The topological charge can be read from the rapid change of the phase, which is defined within $[-\pi : \pi]$. The gas jet is placed at 2 mm after the laser focus.

major ring in the intensity profile with about the same radius for different harmonic orders; see Figs. 3(g)–3(i); thus harmonics are emitted with similar divergence at about 7 mrad. The phase distributions in Figs. 3(j)–3(l) are quite different from those in the near field but the topological charges remain unchanged. The evolution of intensity and phase profiles from near to far fields is mostly due to two factors: one is the focusing effect of the harmonic field which contributes to the phase shift similar to the shift of the Gouy phase; the other is the interference of short- and long-trajectory emissions (discussed in the later sections). Note that the conclusion of similar divergence for different harmonic orders in our simulation is consistent with results from other theory [27] and experiments [21]. These results, however, are different from harmonics generated with Gaussian beams where the divergence changes with the harmonic order [49].

We next inspect the cases when the gas jet is located at and before the laser focus as shown in Figs. 4 and 5, respectively. First, multiple rings can be identified in the intensity distribution in the near field, see Figs. 4(a)–4(c) and Figs. 5(a)–5(c), meaning the existence of a number of radial nodes in the harmonic beams. This also indicates that different phase matching occurs by varying the position of the gas jet. From the phase distributions in Figs. 4(d)–4(f) and

Figs. 5(d)–5(f), we can clearly see the phase jump between rings, but the topological charge does not change with the gas-jet position. Second, in the far field, both intensity and phase profiles reveal extra radial rings, implying that the radial index $p$ is not zero. In addition, the radius of the brightest ring changes with harmonic order, which is different from the case when the gas jet is located after the focus.

In the far field, if the gas jet is before the laser focus, the intensity patterns tend to show a few rings, distinct from that with a single ring where the gas jet is behind the focus. When the gas jet is at the laser focus, the intensity profiles tend to have the most multiple rings. This conclusion is identical to the results in Ref. [39], where full 3D propagation of the harmonic beam in the medium has been taken into account. These results, however, contradict the simulated results in Fig. 2 of Ref. [28]. We suspect that this is due to a different propagation method being implemented in the simulation.

### C. Analysis of phase-matching conditions for OAM harmonics in the gas medium

To explain the dependence of HHG on the gas-jet position, one can either investigate the phase-mismatch conditions of harmonics in terms of coherence length or examine the
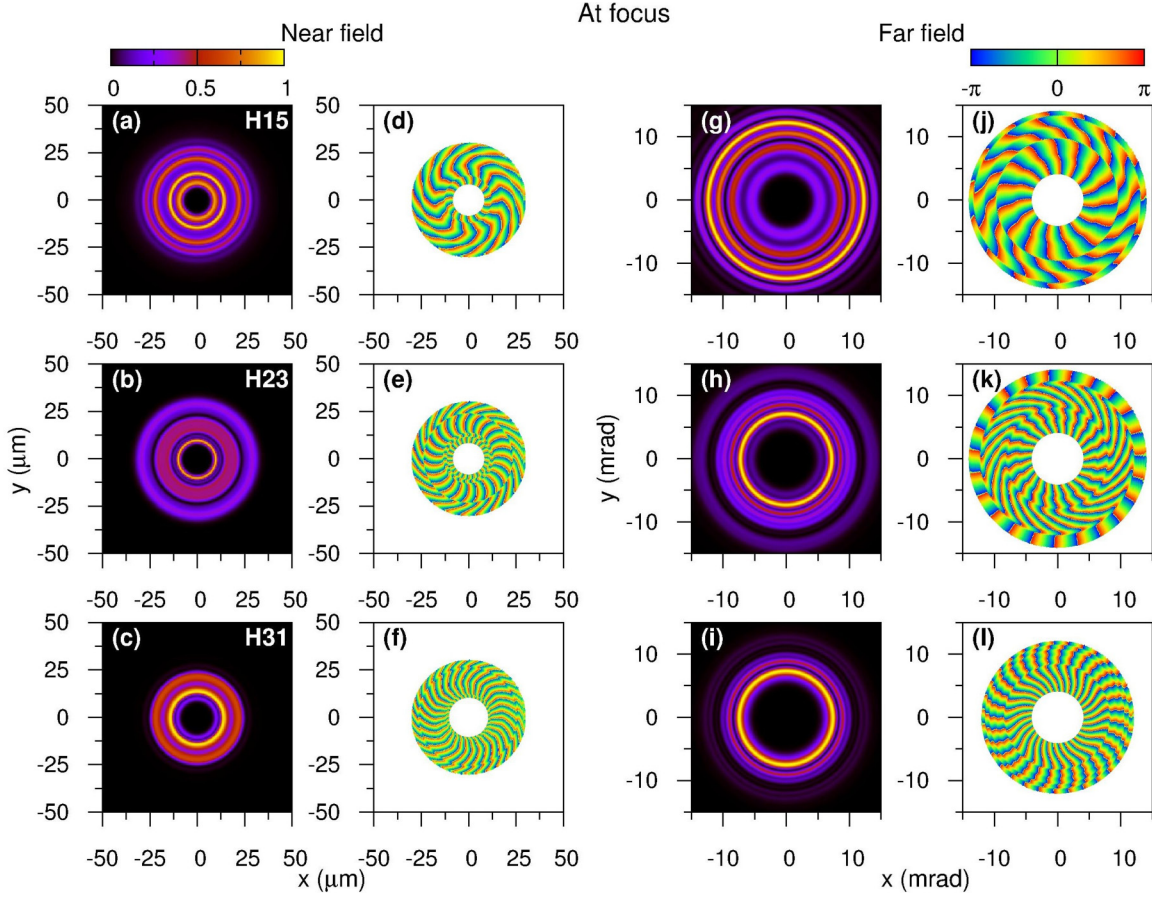
FIG. 4. Same as Fig. 3 except that the gas jet is placed at the laser focus.

accumulation of harmonic strength inside the gas medium. Here we use both approaches to show that they are consistent: the first method is to check the spatial coherence length of harmonics by the analytical formulation of phase mismatch; the second method is to follow the growth of harmonic field in space by solving the 3D Maxwell's wave equations numerically.

### 1. Coherence length of HHG in space

For low intensity and low gas pressure considered in this paper, in the phase-matching analysis we only include the contributions from the spatial phase of driving laser and the intrinsic phase of single-atom response. Other contributions such as neutral atom dispersion and plasma defocusing from free electrons are excluded [50]. Optimum phase matching can be reached when the following condition is satisfied [51–54]:

$$\mathbf{k}_q = q\mathbf{k}_1 + \mathbf{K}, \tag{21}$$

where $\mathbf{k}_q$ is the wave vector of the $q$th harmonic field and $\mathbf{K}$ is from the single-atom response. The total wave vector $\mathbf{k}_1$ for the fundamental LG beam can be expressed as

$$\mathbf{k}_1(r, z) = k_0 \mathbf{e}_z - \nabla \varphi_l(r, \phi, z), \tag{22}$$

where $\mathbf{e}_z$ is the unit vector along the $z$ direction and $k_0 = \omega_0/c$. Note that the sign in front of the term $\nabla \varphi_l$ is negative, which is determined according to the sign convention of the phase

given for the LG beam; see Eq. (11). Since

$$\varphi_l(r, \phi, z) = -k_0 \frac{r^2}{2R(z)} - \zeta(z) - l\phi, \tag{23}$$

$\nabla \varphi_l$ can be written explicitly in cylindrical coordinates as

$$\nabla \varphi_l(r, \phi, z) = \frac{\partial \varphi_l}{\partial r} \mathbf{e}_r + \frac{1}{r} \frac{\partial \varphi_l}{\partial \phi} \mathbf{e}_\phi + \frac{\partial \varphi_l}{\partial z} \mathbf{e}_z$$

$$= \frac{\partial \varphi_l}{\partial r} \mathbf{e}_r - \frac{l}{r} \mathbf{e}_\phi + \frac{\partial \varphi_l}{\partial z} \mathbf{e}_z. \tag{24}$$

Here $\mathbf{e}_r$ and $\mathbf{e}_\phi$ are unit vectors in the $r$ and $\phi$ directions, respectively. Therefore, there is no dependence on the azimuthal angle $\phi$ in Eq. (24). Note that in Ref. [52] the component of wave vector along $\mathbf{e}_\phi$ direction was not included. The effective wave vector $\mathbf{K}$ is used to describe the spatial dependence of the atomic phase as

$$\mathbf{K}(r, z) = \nabla \varphi_{q,\text{dip}}(r, z). \tag{25}$$

Here the intrinsic dipole phase $\varphi_{q,\text{dip}}(r, z)$ is accumulated by an electron in the external field following a specific trajectory. It can be written as

$$\varphi_{q,\text{dip}}(r, z) = -\alpha_i^q I(r, z) = -\alpha_i^q |\varepsilon(r, z)|^2, \tag{26}$$

where $I(r, z)$ is the laser peak intensity. The coefficient of $\alpha_i^q$ depends on short (S) or long (L) trajectories and harmonic order. For harmonics in the plateau, $\alpha_{i=S}^q \approx$
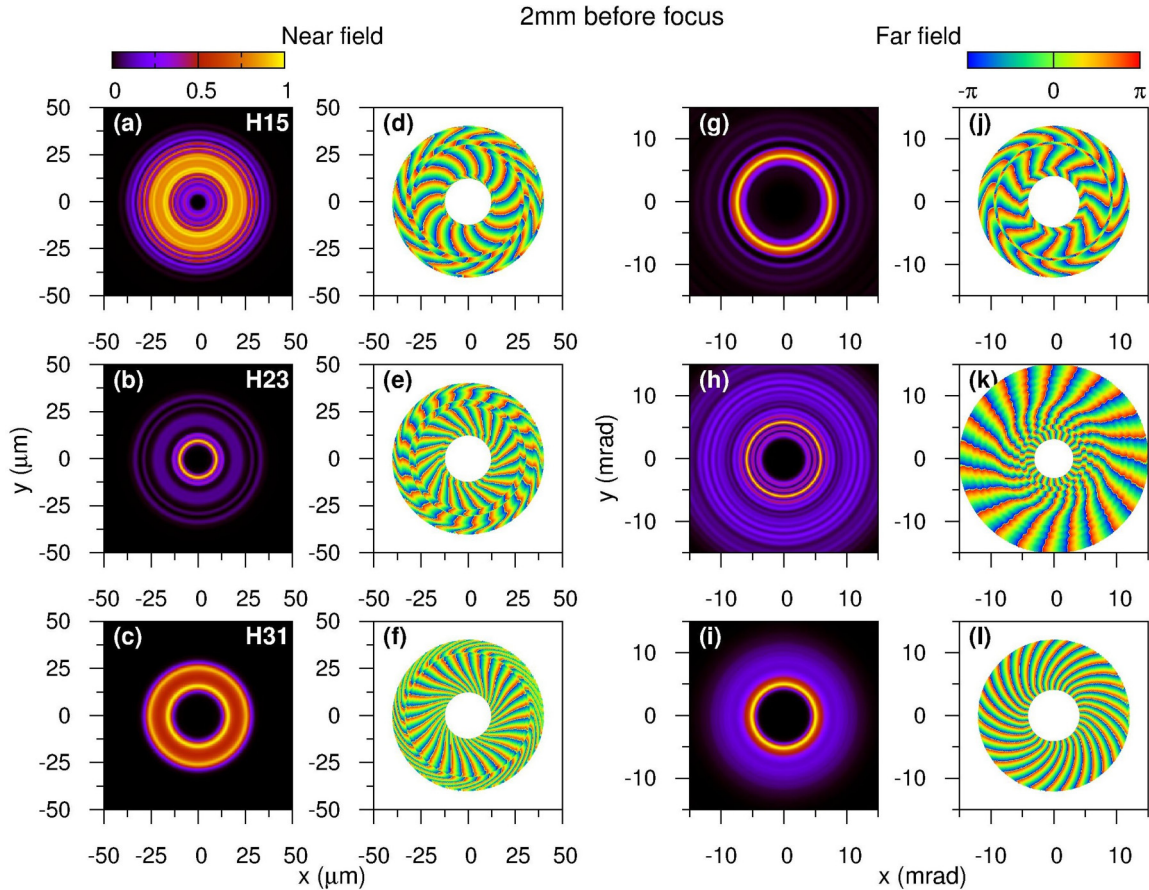
FIG. 5. Same as Fig. 3, but the gas jet is located at 2 mm before the laser focus.

$1 \times 10^{-14}$ rad cm$^2$/W and $\alpha_{i=L}^q \approx 24 \times 10^{-14}$ rad cm$^2$/W. At the cutoff, $\alpha_{i=S,L}^q \approx 13.7 \times 10^{-14}$ rad cm$^2$/W [55,56].

The mismatch of wave vectors between the $q$th harmonic and the fundamental laser can be defined as $\delta\mathbf{k}_q(r, z)$, its direction is along the polarization wave vector $q\mathbf{k}_1 + \mathbf{K}$, and thus its norm is [51]

$$\delta k_q(r, z) = k_q - |q\mathbf{k}_1 + \mathbf{K}|, \qquad (27)$$

with $k_q = q\omega_0/c$. Finally the coherence length can be introduced as

$$L_{q,\text{coh}}(r, z) = \frac{\pi}{|\delta k_q(r, z)|}. \qquad (28)$$

The calculated spatial distributions of coherence length for high harmonics driven by a LG$_{1,0}$ beam are shown on the left column of Fig. 6 where the laser parameters used in the calculations are the same as those in Fig. 1. Since the length of the gas medium is 1 mm, a coherence length in the order of 1 mm or longer can be considered as a condition of good phase matching [51–54]. In the coherent length plots of Fig. 6, we use "white" color to stand for good phase matching where the coherence length is greater than or equal to 1 mm. The intensity distribution of the driving laser is given in Fig. 6(f) as reference. For plateau harmonics, 15th-order harmonic (H15) and H23, the coherence length of short-trajectory harmonic emission depends weakly on the propagation position $z$, with moderately good phase-matching region (light

to dark blue) surrounded by white ones. This region coincides with an off-axis region where the laser intensities are large; see Figs. 6(a), 6(b), and 6(f). But the coherence length varies rapidly with $z$ for long-trajectory harmonic emission. As shown in Figs. 6(d) and 6(e), in the same off-axis region, a narrow phase-matching region appears if $z > 0$; it splits into two regions when $z < 0$. For the cutoff harmonic H31 where long- and short-trajectory emissions coincide, the coherence length has very strong dependence with $z$. From Fig. 6(c), we note that a broad good phase-matching region can be realized off axis (large $r$) if $z > 1.0$ mm. A narrow white region for $z < 1.0$ mm cannot contribute to the cutoff harmonics as a result of small laser intensities.

In Fig. 6, we also show the map of the coherence length of HHG by using a Gaussian beam (or LG$_{0,0}$ mode) for comparison. Note that the scale of the radial direction is half of that shown for the LG$_{1,0}$ beam. The laser intensity distribution, as shown in Fig. 6(i), is much closer to the propagation axis. We can see the big difference in the coherence length map between the two beams. Take the position at $z = 2$ mm for an example. For plateau harmonics, the coherence length is either larger than or close to 1 mm for short-trajectory emissions, while it is much shorter for long-trajectory ones. This is consistent with the general knowledge that short-trajectory harmonic emission can efficiently survive the propagation in the medium if the gas jet is placed after the laser focus.
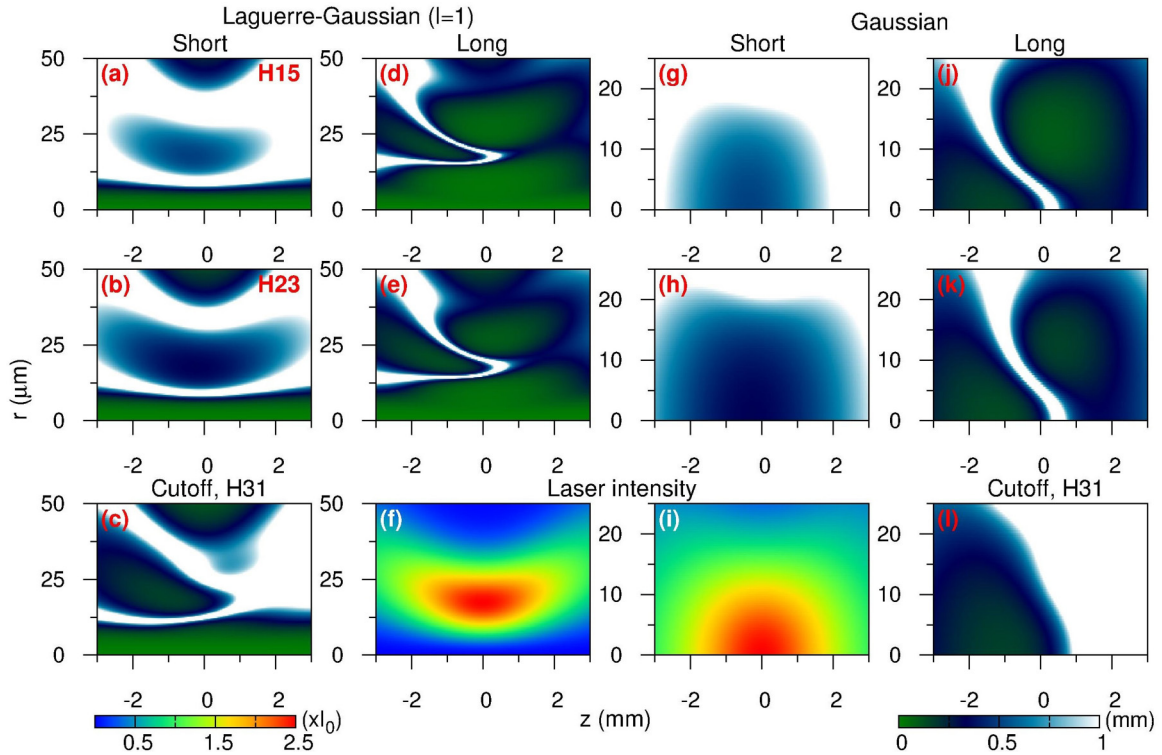
FIG. 6. Map of coherence length for high harmonics along radial and propagation directions driven by $LG_{1,0}$ (left) and Gaussian (right) beams. The laser intensity distributions for the two beams are plotted in (f) and (i) and $I_0 = 10^{14}$ W/cm². First row: H15; second row: H23; third row: H31. For plateau harmonics (H15 and H23), the coherence length is shown in terms of short- or long-trajectory contributions, respectively. H31 is at the cutoff. Note that the "white" area indicates that the coherence length is longer than 1 mm and the scale of the radial distance in the LG beam and Gaussian beams are not the same.

### 2. Evolution of harmonic fields inside the medium

The coherence length map in Fig. 6 reflects the degree of phase matching at each point in the gas medium and it will determine how the harmonic field builds up in the gas medium. The calculated harmonic emissions inside the 1-mm-long medium are displayed along the $z - r$ plane as $z$ increases in Fig. 7 for the three gas-jet locations being considered. Before discussing these results, we first isolate the contribution of emissions due to long-trajectory electrons for plateau harmonics. This is accomplished by truncating the electron excursion time to less than 0.65 optical cycle in the SFA [57,58], thus modifying the electron wave packet used in the QRS model. The resulting harmonic emissions are shown in Fig. 8.

There are some general features that can be easily discerned in Fig. 8. If the exit face of the gas medium $z_{out}$ is before the laser focus, from Figs. 8(a) and 8(b), we can see that the harmonic emissions are converged. If $z_{out}$ is after the laser focus, in accordance with the direction of wave vector of the fundamental laser, the opposite behavior can be seen in Figs. 8(c)–8(f). For H15, there are three emission branches, two narrow ones at the longer and shorter radial positions, respectively, sandwiched with another broader one in between. The middle one is very strong in Fig. 8(e) if the gas jet is located 2 mm after the laser focus because the coherence length is pretty long around $z = 2$ mm in Fig. 6(a). For H23, we also can identify three emission branches. These general

features are slightly dependent on the position of the gas jet, which agrees with the dependence of coherence length on $z$ position as shown in Figs. 6(a) and 6(b). Along the $r$ direction, the split of harmonic emissions is due to the strong intensity dependence of the driving laser [55] as seen in Figs. 6(f).

We then return to take a careful look at Fig. 7, in which both short and long trajectories contribute to the single-atom response. For H15 and H23, the upper and lower emission branches caused by short-trajectory electrons can be clearly identified when the gas jet is before or at the laser focus, and there are additional narrow emission branches between them due to long-trajectory electrons; see Figs. 7(a), 7(b), 7(d), and 7(e). These results strictly follow the change of coherence length in space seen in Figs. 6(d) and 6(e). When the gas jet is after the laser focus, in Figs. 7(g) and 7(h), the interference between short and long trajectories becomes significant, and the two emission branches from short-trajectory electrons either disappear or are weakened. For H31, in Figs. 7(c) and 7(f), the harmonic emissions are gained over short distances. At after-focus jet position, as seen in Fig. 7(i), the harmonic field increases steadily with the propagation distance $z$ over the whole 1 mm length, in agreement with the coherence length in Fig. 6(c).

In short, from the analysis shown in Figs. 7 and 8, we learn the following: (i) for plateau harmonics, when the gas is placed after the laser focus, short and long trajectories strongly interfere in space, resulting in single-ring structure of
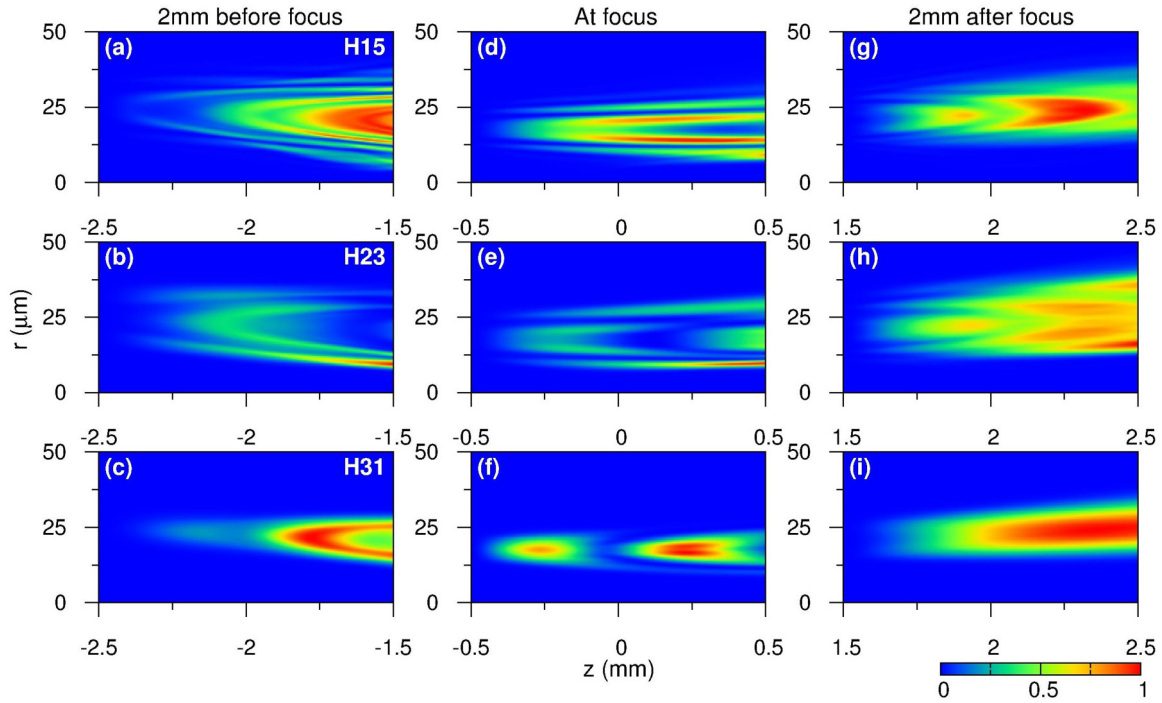
FIG. 7. Evolution of harmonic emissions (normalized) in space for H15 (first row), H23 (second row), and H31 (third row) when a gas jet is placed 2 mm before (first column), at (second column), or 2 mm after (third column) the laser focus. These correspond to near-field harmonics in Figs. 3, 4, and 5.

harmonic emission at the exit plane; (ii) if the gas is located before or at the laser focus, short- and long-trajectory emissions are spatially separated, leading to multiple rings in the intensity distribution of near-field harmonics; (iii) for cutoff harmonics, since there is only one trajectory contributing to emission, the near-field harmonic profile is regular with one relatively narrow ring.

When the gas jet is placed after the laser focus, the divergence in the far field is the same for all harmonic orders as the driving LG laser and is equal to 7 mrad. This can be understood by adopting the analysis used in Ref. [21]. Assuming that each $q$th-harmonic field is described by a given

LG mode ($p = 0$), and is characterized by a scaled beam waist $w_q(z) = w_{0q}\sqrt{1 + (z/z_{0q})^2}$, topological charge $l_q = ql$, as well as other parameters from the fundamental, where the Rayleigh length $z_{0q} = \pi w_{0q}^2/\lambda_q$, with the wavelength $\lambda_q = \lambda_0/q$. Similar to the fundamental laser, the radial position for maximum harmonic intensity (or radius of intensity ring) is given by

$$r_{l_q,\max}(z) = w_q(z)\sqrt{|l_q|/2}. \qquad (29)$$

Since the emission center of the harmonic field from $z = 1.5$ to 2.5 mm appears at the same radial position as the maximum intensity of the fundamental laser, see Figs. 7(g)–7(i) and
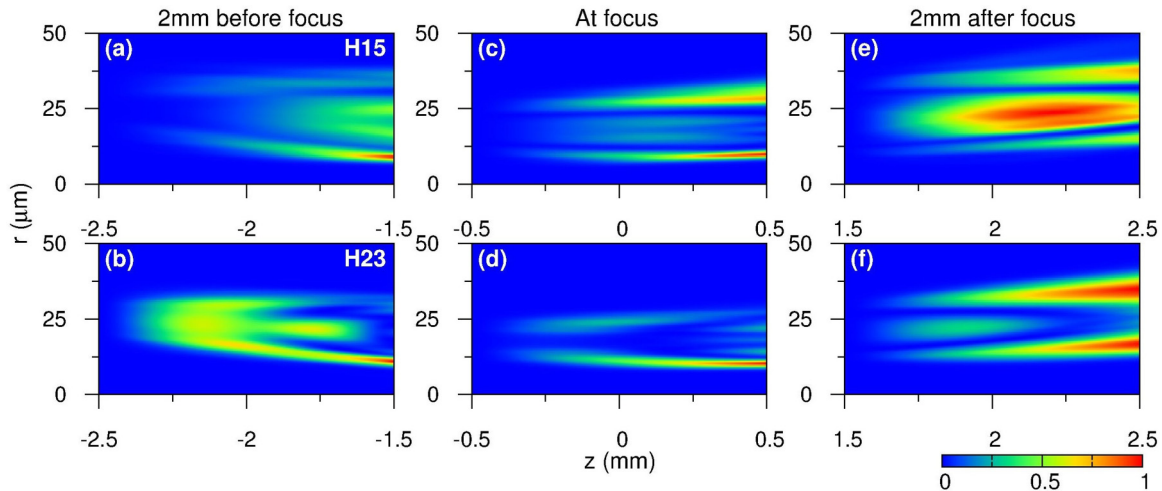


FIG. 8. Same as Fig. 7 but including short-trajectory emissions only.
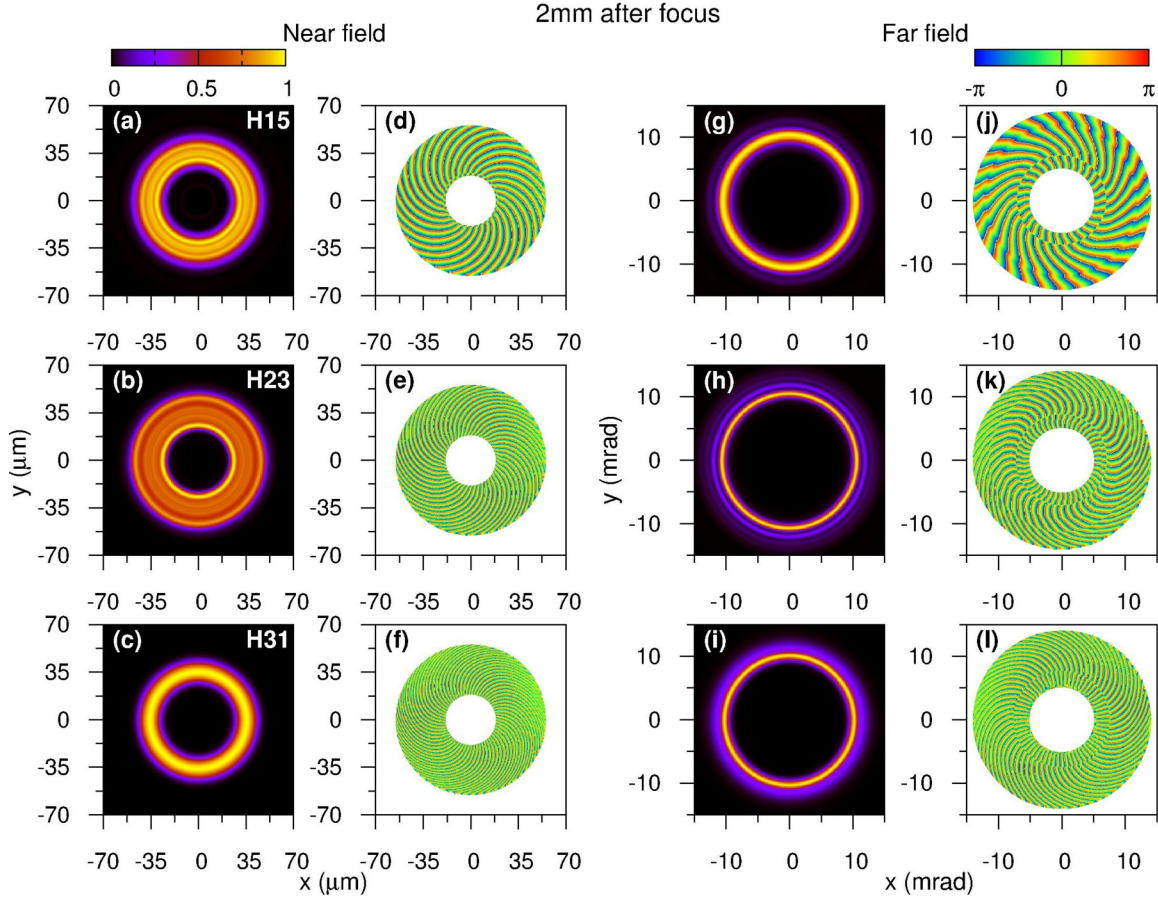
FIG. 9. Same as Fig. 3 but for a driving $LG_{2,0}$ beam.

Fig. 6(f), thus

$$w_0\sqrt{1 + (z/z_0)^2}\sqrt{|l|/2} = w_{0q}\sqrt{1 + (z/z_{0q})^2}\sqrt{|l_q|/2}, \quad (30)$$

for 1.5 mm $\leqslant z \leqslant$ 2.5 mm. One can easily get the following relations:

$$z_0 = z_{0q} \quad (31)$$

and

$$w_0\sqrt{|l|/2} = w_{0q}\sqrt{|l_q|/2}. \quad (32)$$

Therefore, at another propagation position $z >$ 2.5 mm, we have [21]

$$r_{l_q,\max}(z) = w_{0q}\sqrt{1 + (z/z_{0q})^2}\sqrt{|l_q|/2}$$
$$= w_0\sqrt{1 + (z/z_0)^2}\sqrt{|l|/2} = r_{l,\max}(z). \quad (33)$$

In the far field, this equation tells us that the radius of the harmonic intensity ring is the same as that of the fundamental one.

## IV. HIGH HARMONICS GENERATED BY FUNDAMENTAL $LG_{2,0}$ BEAMS

In this section, we check high harmonics generated by a fundamental $LG_{2,0}$ beam. We show the intensity and phase distributions of harmonics in the near and far fields in Fig. 9 with the gas jet being placed 2 mm after the laser focus. One can clearly see that, for all harmonic orders, the intensity

profiles in both near and far fields are quite similar to those generated with the $LG_{1,0}$ beam, but they differ in the spatial range or the divergence angle. The divergence in the far field is about 10 mrad for all the harmonic orders. It is $\sqrt{2}$ times larger than that of the $LG_{1,0}$ beam, which is consistent with the scaling law $\sqrt{|l|}$ of the fundamental. This also agrees with the experimental measurements in Ref. [21], in which the diameter of the intensity ring is proportional to $\sqrt{|l|}$. The azimuthal phase change of harmonics in both the near and far fields demonstrates that the topological charge of the $q$th harmonic is $2q$.

To explain the similarities of the intensity profiles between $LG_{1,0}$ and $LG_{2,0}$ beams, we also look at the phase-matching conditions for high-order harmonics from the $LG_{2,0}$ beam, as shown in Fig. 10. Compared to the $LG_{1,0}$ beam, the change of coherence length with $z$ and its distribution along $r$ are very similar. We also show the evolution of harmonic fields in the medium in Figs. 11(a)–11(c). From these figures, it seems that the small change in coherence length cannot alter the growth of the harmonic fields. The resulting harmonics are almost the replica of those with the $LG_{1,0}$ beam except that emission patterns are shifted in the radial direction.

## V. CONCLUSIONS

In summary, we have presented a thorough study of simulating high-order harmonics generated by intense Laguerre-Gaussian beams with orbital angular momentum (OAM). In
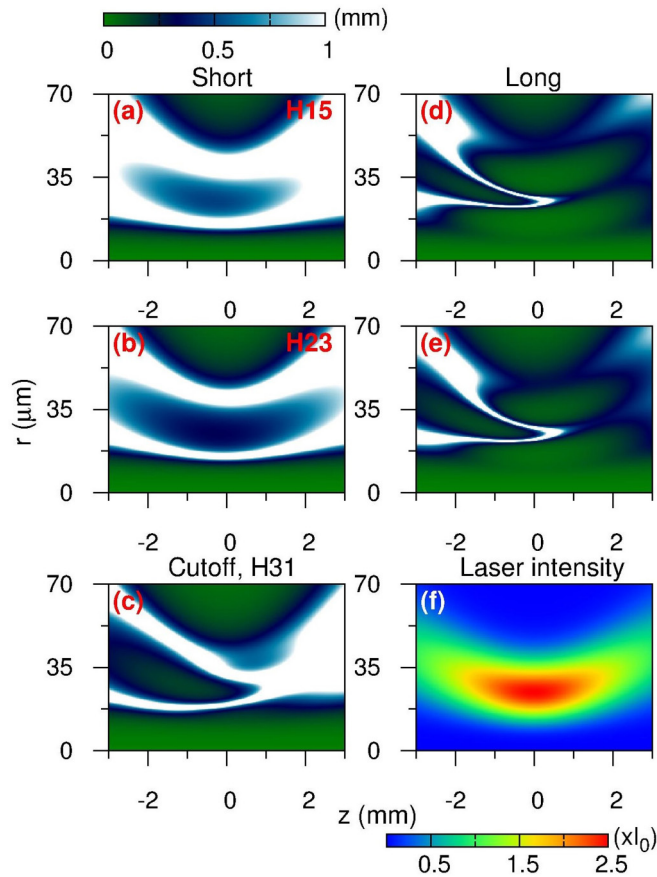
FIG. 10. Same as Fig. 6 but for a driving $LG_{2,0}$ beam.



FIG. 11. Same as Fig. 7 except that the driving laser is a $LG_{2,0}$ beam.

comparison with previous theories, we have solved the 3D Maxwell's wave equations of harmonic field in the medium and applied Huygens' integral to simplify the propagation of harmonic field in vacuum. We have calculated XUV high harmonics using linearly polarized 800 nm OAM beams interacting with Ar gas under tight focusing conditions with low peak intensities in a uniform gas jet at low pressure. The intensity and phase of near- and far-field harmonics have been shown to have strong dependence on the gas-jet position with respect to the laser focus. Detailed phase-matching analysis has been carried out by calculating the coherence length of harmonics in space and by monitoring the buildup of space-dependent harmonic fields in the medium. It has been uncovered that only when the gas medium is placed after the laser focus both short- and long-trajectory electrons contribute to the harmonic emission to result in similar di-

vergence and a single ring intensity profile in the far field. We also have found that the diameter of the intensity ring does not change with the harmonic order and it scales as $\sqrt{|l|}$ with the fundamental topological charge $l$, which is consistent with the experimental finding in Ref. [21]. In the future, further studies would aim at examining the synthesis of OAM-carrying attosecond pulses [21,27,28,59], extending the generation of vortex lights to the soft-x-ray region with mid-infrared lasers [60,61], controlling the topological charge or radial node in the HHG [31,39], and generating high harmonics by using a laser beam with both spin angular momentum and orbital angular momentum [62–64].

[1] Y. Shen, X. Wang, Z. Xie, C. Min, X. Fu, Q. Liu, M. Gong, and X. Yuan, Optical vortices 30 years on: OAM manipulation from topological charge to multiple singularities, Light: Sci. Appl. **8**, 90 (2019).

[2] T. Omatsu, K. Miyamoto, and A. J. Lee, Wavelength-versatile optical vortex lasers, J. Opt. **19**, 123002 (2017).

[3] A. M. Yao and M. J. Padgett, Orbital angular momentum: origins, behavior and applications, Adv. Opt. Photon. **3**, 161 (2011).

[4] A. Picón, A. Benseny, J. Mompart, J. R. Vázquez de Aldana, L. Plaja, G. F. Calvo, and L. Roso, Transferring orbital and spin angular momenta of light to atoms, New J. Phys. **12**, 083053 (2010).

[5] A. Alexandrescu, D. Cojoc, and E. Di Fabrizio, Mechanism of Angular Momentum Exchange Between Molecules and Laguerre-Gaussian Beams, Phys. Rev. Lett. **96**, 243001 (2006).

[6] M. Babiker, C. R. Bennett, D. L. Andrews, and L. C. D. Romero, Orbital Angular Momentum Exchange in the

Interaction of Twisted Light with Molecules, Phys. Rev. Lett. **89**, 143601 (2002).

[7] S. Giri, M. Ivanov, and G. Dixit, Signatures of the orbital angular momentum of an infrared light beam in the two-photon transition matrix element: A step toward attosecond chronoscopy of photoionization, Phys. Rev. A **101**, 033412 (2020).

[8] L. Allen, M. W. Beijersbergen, R. J. C. Spreeuw, and J. P. Woerdman, Orbital angular momentum of light and the transformation of Laguerre-Gaussian laser modes, Phys. Rev. A **45**, 8185 (1992).

[9] D. G. Grier, A revolution in optical manipulation, Nature (London) **424**, 810 (2003).

[10] J. Wang, J.-Y. Yang, I. M. Fazal, N. Ahmed, Y. Yan, H. Huang, Y. Ren, Y. Yue, S. Dolinar, M. Tur, and A. E. Willne, Terabit free-space data transmission employing orbital angular momentum multiplexing, Nat. Photon. **6**, 488 (2012).

[11] A. E. Willner, H. Huang, Y. Yan, Y. Ren, N. Ahmed, G. Xie, C. Bao, L. Li, Y. Cao, Z. Zhao, J. Wang, M. P. J. Lavery, M. Tur, S. Ramachandran, A. F. Molisch, N. Ashrafi, and S. Ashrafi, Optical communications using orbital angular momentum beams, Adv. Opt. Photon. **7**, 66 (2015).

[12] S. Fürhapter, A. Jesacher, S. Bernet, and M. Ritsch-Marte, Spiral interferometry, Opt. Lett. **30**, 1953 (2005).

[13] K. A. Forbes, Raman Optical Activity Using Twisted Photons, Phys. Rev. Lett. **122**, 103201 (2019).

[14] W. Brullot, M. K. Vanbel, T. Swusten, and T. Verbiest, Resolving enantiomers using the optical angular momentum of twisted light, Sci. Adv. **2**, e1501349 (2016).

[15] J. C. T. Lee, S. J. Alexander, S. D. Kevan, S. Roy, and B. J. McMorran, Laguerre–Gauss and Hermite–Gauss soft X-ray states generated using diffractive optics, Nat. Photon. **13**, 205 (2019).

[16] L. Rego, K. M. Dorney, N. J. Brooks, Q. L. Nguyen, C.-T. Liao, J. S. Román, D. E. Couch, A. Liu, E. Pisanty, M. Lewenstein, L. Plaja, H. C. Kapteyn, M. M. Murnane, and C. Hernández-García, Generation of extreme-ultraviolet beams with time-varying orbital angular momentum, Science **364**, eaaw9486 (2019).

[17] C. Hernádez-García, J. Vieira, J. T. Mendonça, L. Rego, J. S. Román, L. Plaja, P. R. Ribic, D. Gauthier, and A. Picón, Generation and applications of extreme-ultraviolet vortices, Photonics **4**, 28 (2017).

[18] D. Gauthier, S. Kaassamani, D. Franz, R. Nicolas, J.-T. Gomes, L. Lavoute, D. Gaponov, S. Février, G. Jargot, M. Hanna, W. Boutu, and H. Merdji, Orbital angular momentum from semiconductor high-order harmonics, Opt. Lett. **44**, 546 (2019).

[19] M. Zürch, C. Kern, P. Hansinger, A. Dreischuh, and Ch. Spielmann, Strong-field physics with singular light beams, Nat. Phys. **8**, 743 (2012).

[20] G. Gariepy, J. Leach, K. T. Kim, T. J. Hammond, E. Frumker, R. W. Boyd, and P. B. Corkum, Creating High-Harmonic Beams with Controlled Orbital Angular Momentum, Phys. Rev. Lett. **113**, 153901 (2014).

[21] R. Géneaux, A. Camper, T. Auguste, O. Gobert, J. Caillat, R. Taïeb, and T. Ruchon, Synthesis and characterization of attosecond light vortices in the extreme ultraviolet, Nat. Commun. **7**, 12583 (2016).

[22] F. Kong, C. Zhang, F. Bouchard, Z. Li, G. G. Brown, D. H. Ko, T. J. Hammond, L. Arissian, R. W. Boyd, E. Karimi, and

P. B. Corkum, Controlling the orbital angular momentum of high harmonic vortices, Nat. Commun. **8**, 14970 (2017).

[23] D. Gauthier, P. R. Ribič, G. Adhikary, A. Camper, C. Chappuis, R. Cucini, L. F. DiMauro, G. Dovillaire, F. Frassetto, R. Géneaux, P. Miotti, L. Poletto, B. Ressel, C. Spezzani, M. Stupar, T. Ruchon, and G. De Ninno, Tunable orbital angular momentum in high-harmonic generation, Nat. Commun. **8**, 14971 (2017).

[24] C. Hernández-García, A. Turpin, J. S. Román, A. Picón, R. Drevinskas, A. Cerkauskaite, P. G. Kazansky, C. G. Durfee, and Í. J. Sola, Extreme ultraviolet vector beams driven by infrared lasers, Optica **4**, 520 (2017).

[25] J. Troß and C. A. Trallero-Herrero, High harmonic generation spectroscopy via orbital angular momentum, J. Chem. Phys. **151**, 084308 (2019).

[26] X. Fan, H.-J. Liang, L.-Y. Shan, B. Yan, Q.-H. Gao, R. Ma, and D.-J. Ding, Extreme ultraviolet polarized vortex light based on high-order harmonic generation, Acta Phys. Sin. **69**, 044203 (2020).

[27] C. Hernández-García, A. Picón, J. S. Román, and L. Plaja, Attosecond Extreme Ultraviolet Vortices from High-Order Harmonic Generation, Phys. Rev. Lett. **111**, 083602 (2013).

[28] C. Hernández-García, J. S. Román, L. Plaja, and A. Picón, Quantum-path signatures in attosecond helical beams driven by optical vortices, New J. Phys. **17**, 093029 (2015).

[29] L. Rego, J. S. Román, A. Picón, L. Plaja, and C. Hernádez-García, Nonperturbative Twist in the Generation of Extreme-Ultraviolet Vortex Beams, Phys. Rev. Lett. **117**, 163202 (2016).

[30] A. Turpin, L. Rego, A. Picón, J. S. Román, and C. Hernádez-García, Extreme ultraviolet fractional orbital angular momentum beams from high harmonic generation, Sci. Rep. **7**, 43888 (2017).

[31] W. Paufler, B. Böing, and S. Fritzsche, Tailored orbital angular momentum in high-order harmonic generation with bicircular Laguerre-Gaussian beams, Phys. Rev. A **98**, 011401(R) (2018).

[32] W. Paufler, B. Böing, and S. Fritzsche, High harmonic generation with Laguerre-Gaussian beams, J. Opt. **21**, 094001 (2019).

[33] M. Geissler, G. Tempea, A. Scrinzi, M. Schnürer, F. Krausz, and T. Brabec, Light Propagation in Field-Ionizing Media: Extreme Nonlinear Optics, Phys. Rev. Lett. **83**, 2930 (1999).

[34] E. Priori, G. Cerullo, M. Nisoli, S. Stagira, S. De Silvestri, P. Villoresi, L. Poletto, P. Ceccherini, C. Altucci, R. Bruzzese, and C. de Lisio, Nonadiabatic three-dimensional model of high-order harmonic generation in the few-optical-cycle regime, Phys. Rev. A **61**, 063801 (2000).

[35] Z. Chang, Single attosecond pulse and XUV supercontinuum in the high-order harmonic plateau, Phys. Rev. A **70**, 043802 (2004).

[36] V. Tosa, H. T. Kim, I. J. Kim, and C. H. Nam, High-order harmonic generation by chirped and self-guided femtosecond laser pulses. I. Spatial and spectral analysis, Phys. Rev. A **71**, 063807 (2005).

[37] M. B. Gaarde, J. L. Tate, and K. J. Schafer, Macroscopic aspects of attosecond pulse generation, J. Phys. B **41**, 132001 (2008).

[38] C. Jin, A. T. Le, and C. D. Lin, Medium propagation effects in high-order harmonic generation of Ar and $N_2$, Phys. Rev. A **83**, 023411 (2011).

[39] R. Géneaux, C. Chappuis, T. Auguste, S. Beaulieu, T. T. Gorman, F. Lepetit, L. F. DiMauro, and T. Ruchon, Radial index

of Laguerre-Gaussian modes in high-order-harmonic generation, Phys. Rev. A **95**, 051801(R) (2017).

[40] C. Zhang, E. Wu, M. Gu, and C. Liu, Propagation effects in the generation process of high-order vortex harmonics, Opt. Express **25**, 21241 (2017).

[41] A. Picón, J. Mompart, J. R. Vázquez de Aldana, L. Plaja, G. F. Calvo, and L. Roso, Photoionization with orbital angular momentum beams, Opt. Express **18**, 3660 (2010).

[42] C. Jin, A. T. Le, and C. D. Lin, Retrieval of target photorecombination cross sections from high-order harmonics generated in a macroscopic medium, Phys. Rev. A **79**, 053413 (2009).

[43] C. D. Lin, A. T. Le, C. Jin, and H. Wei, in *Attosecond and Strong-Field Physics: Principles and Applications* (Cambridge University Press, Cambridge, UK, 2018), pp. 56–58.

[44] A. T. Le, R. R. Lucchese, S. Tonzani, T. Morishita, and C. D. Lin, Quantitative rescattering theory for high-order harmonic generation from molecules, Phys. Rev. A **80**, 013401 (2009).

[45] C. D. Lin, A. T. Le, C. Jin, and H. Wei, Elements of the quantitative rescattering theory, J. Phys. B **51**, 104001 (2018).

[46] N. Abro, K. Wang, X. Zhu, B. Li, and C. Jin, Improvement of the ionization factor in the quantitative rescattering theory for simulating macroscopic high-order harmonic generation, Phys. Rev. A **98**, 023411 (2018).

[47] M. V. Ammosov, N. B. Delone, and V. P. Krainov, Tunnel ionization of complex atoms and of atomic ions in an alternating electromagnetic field, Zh. Eksp. Teor. Fiz. **91**, 2008 (1986) [Sov. Phys. JETP **64**, 1191 (1986)].

[48] X. M. Tong and C. D. Lin, Empirical formula for static field ionization rates of atoms and molecules by lasers in the barrier-suppression regime, J. Phys. B **38**, 2593 (2005).

[49] F. Catoire, A. Ferré, O. Hort, A. Dubrouil, L. Quintard, D. Descamps, S. Petit, F. Burgy, E. Mével, Y. Mairesse, and E. Constant, Complex structure of spatially resolved high-order-harmonic spectra, Phys. Rev. A **94**, 063401 (2016).

[50] C. Jin and C. D. Lin, Comparison of high-order harmonic generation of Ar using truncated Bessel and Gaussian beams, Phys. Rev. A **85**, 033423 (2012).

[51] Ph. Balcou, P. Salières, A. L'Huillier, and M. Lewenstein, Generalized phase-matching conditions for high harmonics: The role of field-gradient forces, Phys. Rev. A **55**, 3204 (1997).

[52] W. Paufler, B. Böing, and S. Fritzsche, Coherence control in high-order harmonic generation with Laguerre-Gaussian beams, Phys. Rev. A **100**, 013422 (2019).

[53] L. E. Chipperfield, P. L. Knight, J. W. G. Tisch, and J. P. Marangos, Tracking individual electron trajectories in a high harmonic spectrum, Opt. Commun. **264**, 494 (2006).

[54] C. Altucci, R. Bruzzese, C. de Lisio, M. Nisoli, E. Priori, S. Stagira, M. Pascolini, L. Poletto, P. Villoresi, V. Tosa, and K. Midorikawa, Phase-matching analysis of high-order harmonics generated by truncated Bessel beams in the sub-10-fs regime, Phys. Rev. A **68**, 033806 (2003).

[55] M. Lewenstein, P. Salières, and A. L'Huillier, Phase of the atomic polarization in high-order harmonic generation, Phys. Rev. A **52**, 4747 (1995).

[56] M. B. Gaarde and K. J. Schafer, Quantum path distributions for high-order harmonics in rare gas atoms, Phys. Rev. A **65**, 031406(R) (2002).

[57] M. Lewenstein, P. Balcou, M. Y. Ivanov, A. L'Huillier, and P. B. Corkum, Theory of high-harmonic generation by low-frequency laser fields, Phys. Rev. A **49**, 2117 (1994).

[58] A.-T. Le, H. Wei, C. Jin, and C. D. Lin, Strong field approximation in high-order harmonic generation with mid-infrared lasers, J. Phys. B **49**, 053001 (2016).

[59] M. A. Porras, Attosecond helical pulses, Phys. Rev. A **100**, 033826 (2019).

[60] J. Qian, Y. Peng, Y. Li, P. Wang, B. Shao, Z. Liu, Y. Leng, and R. Li, Femtosecond mid-IR optical vortex laser based on optical parametric chirped pulse amplification, Photon. Res. **8**, 421 (2020).

[61] H. Tong, G. Xie, Z. Qiao, Z. Qin, P. Yuan, J. Ma, and L. Qian, Generation of a mid-infrared femtosecond vortex beam from an optical parametric oscillator, Opt. Lett. **45**, 989 (2020).

[62] P.-C. Huang, C. Hernández-García, J.-T. Huang, P.-Y. Huang, C.-H. Lu, L. Rego, D. D. Hickstein, J. L. Ellis, A. Jaron-Becker, A. Becker, S.-D. Yang, C. G. Durfee, L. Plaja, H. C. Kapteyn, M. M. Murnane, A. H. Kung, and M.-C. Chen, Polarization control of isolated high-harmonic pulses, Nat. Photon. **12**, 349 (2018).

[63] E. Pisanty, L. Rego, J. S. Román, A. Picón, K. M. Dorney, H. C. Kapteyn, M. M. Murnane, L. Plaja, M. Lewenstein, and C. Hernández-García, Conservation of Torus-Knot Angular Momentum in High-Order Harmonic Generation, Phys. Rev. Lett. **122**, 203201 (2019).

[64] K. M. Dorney, L. Rego, N. J. Brooks, J. S. Román, C.-T. Liao, J. L. Ellis, D. Zusin, C. Gentry, Q. L. Nguyen, J. M. Shaw, A. Picón, L. Plaja, H. C. Kapteyn, M. M. Murnane, and C. Hernández-García, Controlling the polarization and vortex charge of attosecond high-harmonic beams via simultaneous spin-orbit momentum conservation, Nat. Photon. **13**, 123 (2019).